Bridging the shocked monazite gap- Deformation microstructures in natural and laser shock-loaded samples.

A.-M. Seydoux-Guillaume[1], T. de Resseguier[2], G. Montagnac[3], S. Reynaud[4], H. Leroux[5], B. Reynard[3] and A. J. Cavosie[6].

[1] Univ Lyon, UJM, UCBL, ENSL, CNRS, LGL-TPE, F-42023 Saint Etienne, France

[2] PPRIME, CNRS-ENSMA-Université de Poitiers, 1 avenue Clément Ader, 86961 Futuroscope, France

[3]Univ Lyon, ENSL, UCBL, UJM, CNRS, LGL-TPE, F-69007 Lyon, France

[4] Université de Lyon, UJM-Saint-Etienne, CNRS, Institut d'Optique Graduate School, Laboratoire Hubert Curien UMR 5516, F-42023 Saint-Etienne, France

[5] Univ. Lille, CNRS, INRAE, Centrale Lille, UMR 8207 - UMET - Unité Matériaux et Transformations, F-59000 Lille, France

[6]The Space Science and Technology Centre (SSTC) and the Institute for Geoscience Research (TIGeR), School of Earth and Planetary Science, Curtin University, Perth, WA 6102, Australia

Keywords: Shock metamorphism – Monazite – Laser-shock experiments - Transmission Electron Microscope – Vredefort impact

ABSTRACT

Impact-related damage in minerals and rocks provides key evidence to identify impact structures, and deformation of U-Th-minerals in target rocks, such as monazite, makes possible precise dating and determination of pressure-temperature conditions for impact events. Here a laser-driven shock experiment using a high-energy laser pulse of ns-order duration was carried out on a natural monazite crystal to compare experimentally produced shock-deformation microstructures with those observed in naturally shocked monazite. Deformation microstructures from regions that may have experienced up to ~50 GPa and 1000°C were characterized using Raman spectroscopy and transmission electron

microscopy. Experimental results were compared with nanoscale observations of deformation microstructures found in naturally shocked monazite from the Vredefort impact structure (South Africa). Raman-band broadening observed between unshocked and shocked monazite, responsible for a variation of ~3 cm^{-1} in the FWHM, is interpreted to result from the competition between shock-induced distortion of the lattice, and post-shock annealing. At nanoscale, two main plastic deformation structures were found in experimentally shocked monazite: mosaïcism, and deformation bands. In contrast, the naturally shocked monazite sample, contained only deformation twins with elemental enrichment along host-twin boundaries. Both mosaicism and deformation bands, expressed in SAED patterns as streaking of spots, and the presence of extra spots (more or less pronounced), are proposed as nano-scale signatures of shock metamorphism in monazite. Experimentally calibrated deformation features, such as those documented here at TEM-scale, provide new tools for identifying evidence of shock deformation in natural samples.

1. INTRODUCTION

The formation of meteorite impact craters is a ubiquitous process on planetary surfaces (*French and Koeberl, 2010*). On Earth, few impact craters are accurately and precisely dated due to the lack of suitable age geochronometers (*Schmieder and Kring, 2020*), which makes it difficult to link meteorite impacts to significant events in the geological record (*Jourdan et al., 2012*). As a result, fundamental questions regarding possible links between impact events, changes in the geosphere and biosphere, and the origin of life, all of which rely on the acquisition of both accurate impact conditions and timing, remain debated (*Moser et al., 2019*).

Impact-related damage in minerals and rocks provides key evidence to identify impact structures (*French and Koeberl, 2010*). Shock deformation microstructures have been intensively studied in some minerals, especially quartz, down to the nanometer scale with transmission electron microscopy (TEM), and include formation of dislocations, planar deformation features (PDF), mosaïcism (i.e. a mosaic texture with small domains of crystalline blocks slightly misoriented to each

other), twins, high-pressure phases, decomposition, recrystallization, and melting (*e.g., Leroux et al., 1994*). Their formation initially depends on pressure conditions, often above 10 GPa, are attained within nanoseconds to seconds (*Langenhorst and Deutsch, 2012*), and can be modified by subsequent heating. Over the past decade, with the advent of high-spatial resolution techniques, resolving deformation of U-Th-minerals in target rocks (e.g. zircon, monazite, apatite, xenotime, titanite) makes possible precise dating and determination of pressure-temperature conditions (P,T) for impact events. Zircon is the most widely studied geochronometer for shock deformation and forms various shock microstructures (*e.g. Wittmann et al., 2006; Moser et al., 2011; Timms et al. 2017*). In contrast, shocked monazite is less studied; neoblasts (*Erickson et al., 2017; Erickson et al., 2020)*, deformation twins (*Erickson et al., 2016; Fougerouse et al., 2021a*), and a high-pressure phase (Erickson et al., 2019) can form during shock metamorphism, all of which offer the potential for dating impacts. One important drawback of zircon concerns self-irradiation damage that can lead to complete amorphization (*Ewing et al., 2003*). This has consequences both on the disturbance of the U-Pb geochronological systems (e.g. *Seydoux-Guillaume et al., 2015; Peterman et al., 2016*), and also on formation and retention of deformation microstructures. For example, radiation damage can inhibit the formation of the high-pressure phase reidite (*Lang et al., 2008; Timms et al., 2018*), and obliterate shock microstructures at atom scale over time (*Reimold et al., 2002*). In contrast, despite a much higher radionuclide incorporation capacity, monazite is much more resistant to irradiation. Monazite has the ability to remain crystalline over geological time due to self-annealing of radiation damage (*Seydoux-Guillaume et al. 2004; 2018*), and can therefore preserve more or less the same structural state upon impact. In this regard, reliable impact conditions may be more readily extracted from shock-features in monazite over time (e.g. *Erickson et al., 2020*).

Published studies show that evidence of impact age resetting in U-Pb geochronometers can be highly heterogeneous due to complex microstructures at the grain scale (*e.g. Cavosie et al., 2018 and 2021*). Shock-deformation in monazite has previously been described (*Schärer and Deutsch, 1990)*, however its microstructure has only been systematically described at the micrometer scale

recently using electron backscatter diffraction (EBSD) (*Erickson et al., 2016, 2017, 2020; Cavosie et al., 2018*). No nanometer-scale investigations using TEM to describe shock deformation features in monazite have been conducted previously.

Experimental approaches have been applied to address formation of shock deformation microstructures in monazite (*Deutsch and Schärer, 1990; Huang et al., 2010; Lacomba-Perales et al., 2010; Seydoux-Guillaume et al., 2010; D'Abzac et al., 2012*; *Heuser et al., 2018),* and some propose the existence of high-pressure monazite polymorphs which have thus far not been discovered in nature (*Erickson et al., 2019*). Laser-driven experiments have previously demonstrated the ability to simulate conditions of impact events (e.g. in olivine; *Langenhorst et al., 1999*). Here we compare nanoscale deformation structures formed in shocked monazite from the Vredefort impact structure in South Africa (*Cavosie et al., 2018*) with experimentally shocked monazite, in order to identify which features can be used as shock indicators, and also enhance the validity of laser-driven shock-experiments.

2. Materials and Methods

2.1. Starting material

A piece of a centimeter-sized single monazite crystal from Manangotry (Madagascar) was cut in a random orientation, embedded in epoxy and polished (Fig. 1). The sample was previously structurally characterized at the nanoscale by TEM (*Seydoux-Guillaume et al., 2004; Grand'Homme et al., 2018*), particularly with regards to structural defects induced by radiation damage; no twins were observed in previous studies. This monazite crystal is also chemically homogenous, with negligible inclusions and porosity, and has a well-resolved age (555 ± 2 Ma, ID-TIMS; *Paquette and Tiepolo, 2007*).

A shocked monazite grain from the Rietputs Formation in South Africa (Sample Sec-03D, grain 9) was also investigated to evaluate if laser-driven shock experiments are able to reproduce impact damage found in nature. This monazite is a detrital grain that eroded from shocked bedrock at the

Vredefort impact structure, and was transported ~500 km downstream in the Vaal River (*Cavosie et al., 2018*). It was previously characterized with BSE and EBSD, and shown to contain an anomalously high density of deformation twins, as well as localized areas that have recrystallized into neoblastic domains (*Cavosie et al., 2018*). The original host rock is unknown, however, it is assumed that the detrital shocked monazite originated from between the 20 and 30 GPa isobars at the Vredefort impact structure, as it is not fully neoblastic (e.g., *Erickson et al., 2017*), and is similar to other detrital shocked monazite grains that host shock-twinned zircon inclusions (*Erickson et al., 2016*).

2.2. Laser-driven shock loading

The laser shock experiment was carried out at the "nano2000" facility of the *Laboratoire pour l'Utilisation des Lasers Intenses* (LULI, UMR CNRS 7605, Ecole Polytechnique, Palaiseau, France). The target consisted of a 20 µm-thick Al foil glued on top of the monazite crystal (Fig. 1a). A high-power laser pulse of 1.06 µm-wavelength, 5 ns-duration, 765 J-energy, was focused onto a 3.2 mm-diameter spot on the target surface. The resulting laser intensity was about 1.9×10^{12} W/cm². A thin absorbing layer of Al (~µm-order) is ablated into a plasma cloud, whose expansion drives a short compressive pulse. The amplitude (50 GPa) of this pressure pulse and its temporal shape (about 6 ns-duration at half maximum) were inferred from a simulation of laser-matter interaction, using the measured profile of laser intensity as an input boundary condition. Shock pressure transmitted to the monazite sample across the Al-monazite interface was estimated by accounting for the impedance mismatch between both materials, using data reported for $CePO_4$ monazite (*Feng et al., 2013; Du et al. 2009*). Peak loading pressure applied on the monazite crystal was thus calculated at 56.7 GPa. The post-shock temperature computed in Al is about 1300 K, which agrees with calculated thermodynamic data for a 50 GPa mean shock pressure (*Kinslow, 1970*). The subsequent post-release temperature in Al after pressure unloading is about 700 K. In the monazite crystal however, shock-induced heating cannot be assessed without an equation of state for this material, but it should be similar in a natural impact event for an

analogous loading pressure, as temperature only depends on shock pressure. Nevertheless, the much shorter during of both pressure and temperature under laser-driven compression may result in differences in shock-induced transformations, due to (i) possible kinetic inhibition of time-consuming processes (e.g. diffusion, conduction), and (ii) faster pressure decay with propagation distance which would strongly restrict the size of the shock-heated region and possibly hinder neighbourhood effects within heterogeneous samples. One goal of this study is thus to address both relevance and limitations of the impact/laser analog.

2.3. Analytical methods.

Raman spectra were collected directly on the shocked surface of the monazite crystal in clean areas (Fig. 1d-g) with a Horiba micro-Raman spectrometer LabRam HR800 evolution. Groups of 10 spectra were collected respectively on starting material, shocked samples C1 and C2, with two accumulations of 10 s exposure (Fig. 2a). Raman peaks were fitted with Gauss-Lorentz spectral models in the spectral range from 800 to 1200 cm^{-1}, with the Matlab application tool PeakFit to extract the position and full width at half maximum (FWHM) of the v_1 peak (Fig. 2b, Table S1). FWHM values are corrected for the apparatus function of the Raman instrument (*Nasdala et al., 2001*).

The TEM foils were prepared using a Thermo Fisher Scientific FEI 125 Helios Nanolab 600i focused-ion beam scanning electron microscope (FIB/SEM) hosted by MANUTECH USD platform, at Hubert Curien laboratory, Saint-Etienne (France). Nanoscale characterization was performed with a Cs-corrected TEM (NeoARM200F Cold FEG) at 200 kV, operated by the CLYM and hosted within the Hubert Curien Laboratory, Saint-Etienne (France). A Gaussian low-pass filter for noise reduction was applied to high-magnification STEM images (Figures 5c-d, 8d-f and 9d).

For further details see Supplementary Materials.

3. RESULTS

154 *3.1. Optical and SEM observations*

155 After the shock experiment the Al-foil was removed but some glue remained on the surface
156 (dark areas in Figure 1d and also SEM images in figures 1f and g, rough zones on the surface). Only
157 domains free of glue were targeted for analysis (Raman and TEM), i.e. zones C1 and C2. In optical light
158 the central zone is a rounded area where the shock was most intense (Fig. 1b-d); it is approximately 3
159 mm in diameter, which matches the 3.2 mm-diameter of the irradiated spot in the Al foil (Fig. 1b).
160 Numerous planar fractures in monazite are visible in this area, with at least two directions nearly
161 perpendicular to each other (arrows in Fig. 1 c-g). Some of the planar microstructures appear open
162 (Fig. 1c and g), and thus may be tensile fractures.

163

164 *3.2. Raman observations*

165 Raman measurements were performed on both unshocked areas of the monazite crystal and
166 in the central shocked zone (C1 and C2; Fig. 1). The first result is that only monazite was identified; no
167 peaks associated with other phases were present. As described in *Heuser et al. (2018),* bands between
168 900 and 1100 cm^{-1} can be assigned to antisymmetric (ν_3) and symmetric (ν_1) stretching modes,
169 respectively, and peaks between 400 and 700 cm^{-1} to antisymmetric (ν_4) and symmetric (ν_2) bending
170 modes of the PO_4 group of monazite. Differences between the three areas are apparent only in the
171 position and shape of the peaks. As previously shown (*Seydoux-Guillaume et al., 2002; Ruschel et al.,*
172 *2012*) the FWHM of the ν_1 Raman band is suitable to estimate the degree of short-range order of
173 monazite (Fig. 2b). Mean values for the position vary from 969.40 cm^{-1} for unshocked monazite to
174 968.81 and 968.34 cm^{-1} for shocked monazite (C1 and C2 zones respectively), and for FWHM from
175 18.34 (unshocked monazite) to 21.52 and 21.45 cm^{-1} (C1 and C2 respectively). The positions and
176 FWHM are more variable in shocked areas (968.62-968.93/21.20-21.94 cm^{-1} for C1, 968.13-
177 968.57/21.09-21.93 cm^{-1} for C2) than unshocked areas (969.30-969.51/18.10-18.73 cm^{-1}) of the
178 crystal, indicating a higher local variability of microstructure.

179

180 *3.3. Transmission Electron Microscopy*

181 Nanoscale characterization was conducted on two TEM foils extracted from the central part
182 of the shocked monazite sample: one in area C1 (FIB1), and one in area C2 (FIB5), a little further from
183 the center of the shocked zone (Fig. 1). Both foils allow observations to be made over approximately
184 8 µm of depth, from the surface to the interior of the monazite crystal. In the following sections (3.3.1
185 and 3.3.2) different deformation structures induced by laser-driven shock loading are described. One
186 TEM foil was also prepared from the naturally shocked monazite grain from Vredefort for comparison
187 (Fig. 8), and deformation structures are described in section 3.3.3.

188 Each monazite sample reveals typical contrasts in bright-field (BF) TEM mode due to radiation
189 damage (*Seydoux-Guillaume et al., 2004*). The starting (i.e. unshocked) monazite sample as well shows
190 typical mottled diffraction contrasts due to the presence of a distorted lattice (*Seydoux-Guillaume et*
191 *al., 2002*). The diffraction contrasts are a consequence of the competition between defect formation
192 and annealing of radiation damage (*Seydoux-Guillaume et al., 2018*). However, the distortion is not
193 sufficient to induce visible stretching of diffraction spots (see *Seydoux-Guillaume et al., 2004*), and
194 therefore implies an absence of mosaïcism.

195

196 *3.3.1. TEM foil C1 (FIB1) – Figures 3 to 5*

197 Deformation features in foil FIB1-C1 vary spatially depending on the depth of observation
198 within the foil relative to the polished surface (Figures 3-5). From the surface of the sample down to
199 approximately 3 µm (Fig. 3b), FIB1 is characterized by mosaicism, which consists of a high density of
200 ~50 nm sized irregularly shaped domains that are slightly misoriented (1-2°) with respect to each
201 other, resulting in a mottled diffraction contrast in BF-TEM (Fig. 3) and a slight streaking of spots in
202 the selected area electron diffraction patterns (SAED; Fig. 3a). Mosaicism indicates the presence of
203 misoriented subgrains, which are ~50 nm-size bright domains visible in Dark-Field (DF) TEM mode (Fig.
204 3c). When the FIB1 foil is oriented parallel to the [100] zone axis (Fig. 3a), extra spots compatible with
205 the monazite structure are visible (DF1 at 3.26Å and DF2 at 1.81Å). At depths below 3 µm from the

surface within foil FIB1 (Fig. 4) the structure is dominated by bands that are subparallel to the surface (Fig. 4a-b), and they are also visible as a SW-NE fabric in the Dark-Field (DF) image (Fig. 4d). The bands are 100-300 nm long and about 50 nm wide, and form a wavy pattern within the sample. Contrast within the bands is quite homogeneous, with a grey color and almost no Bragg contrast, consistent with diminished crystallinity relative to other areas. An SAED pattern (Fig. 4c) across one band in the [100] zone axis shows streaking of some spots, more pronounced than in Fig. 3a, and extra spots (DF1: 3.26Å, DF2: 1.81Å, DF3: 2.06Å). The SAED data are compatible with a monazite structure, and provide evidence of highly disoriented domains (misoriented subgrains are visible in DF-TEM in Fig. 4d-f). Moiré fringes are also observed and provide further evidence of misorientation of the nano-domains (arrows in Fig. 4b). Annular dark field (ADF) scanning TEM (STEM) images across band domains (Fig. 5) show that Bragg contrasts are strongly reduced inside bands (darker areas), resulting from the lower density of the material within the deformation band (Fig. 5a-b). At very high magnification (Fig. 5c-d) the atomic arrangement within the monazite structure is revealed. In ADF mode, only the heaviest atoms are visible (i.e. rare earth elements like Ce in $CePO_4$ monazite structure); in Figure 5f the pattern matches the arrangement of Ce atoms in monazite along the [100] direction. In contrast, within the deformation bands (upper parts in Fig. 5c-d) the atomic arrangement almost disappears, and instead consists of highly disoriented nano-crystals of monazite (some fringes can be observed within these bands).

3.3.2. TEM foil C2 (FIB5) – Figures 6 to 8

In this sample two kinds of deformation features were observed, depending on depth of observation within the foil. From the surface down to approximately 4 µm (Fig. 6a), the sample revealed a high density of 10-20 nm domains that are slightly misoriented with respect to each other, resulting in mottled diffraction contrasts in BF-TEM (Fig. 6a-b). Selected area electron diffraction patterns (SAED) show a slight stretching of diffraction spots (Fig. 6c and e), indicative of a small misorientation of domains (<2 degrees). When the crystal is oriented parallel to the [100] zone axis,

232 the most intense stretching is seen along the (012) plane. Additional diffuse spots are also visible
233 (arrows in Fig. 6e) and are measured at a distance of 3.16 Å, compatible with the monazite structure.
234 At higher magnification moiré fringes (arrows in Fig. 6d) are observed and provide further evidence of
235 misorientation of the nano-domains. From 4 µm depth to the bottom of the foil (Fig. 7a), the structure
236 is dominated by bands subparallel to the shock-loaded surface (Fig. 7b). The bands are 300 ± 50 nm
237 long and about 50 nm wide, are relatively regular, and form a wavy pattern within the sample (Fig. 7
238 c-d). Contrast within the bands is homogeneous, with a grey color, and almost no Bragg contrast,
239 consistent with a low crystallinity, almost glassy structure. An SAED pattern parallel to the [100] zone
240 axis that overlaps a deformation band and the adjacent monazite confirms the presence of a diffuse
241 ring, characteristic of amorphous material that is superimposed on the monazite diffraction signature.
242 The same SAED pattern also revealed the appearance of additional spots, some close to the principal
243 spots from the [100] zone axis (Fig. 7e). The most visible additional spots in the SAED pattern, with the
244 shortest distance, are indicated by arrows in Figure 7e, and correspond to a d_{hkl} of 3.58 Å, close to the
245 distance measured in the part of foil closer to the polished surface (Fig. 6e). Additional spots at 2.59,
246 2.17, 2.01, 1.80 Å are all compatible with the monazite lattice. The same region was observed using
247 scanning TEM (STEM) with an annular dark field (ADF) detector (Fig. 8). In this mode, Bragg contrasts
248 are strongly reduced and contrast arises from atomic number and density. The bands appear darker
249 (Fig. 8a-e) due to the lower density of the glassy material within the deformation band (Fig. 8a-b). At
250 very high magnification (Fig. 8e-f) the atomic arrangement within the monazite structure is revealed,
251 and in Figure 8f the pattern matches the arrangement of Ce atoms in monazite along the [100]
252 direction. High resolution STEM imaging and associated Fast Fourier Transform (FFT; Fig. 8c-e) show
253 that the deformation bands are not completely amorphous, and contain highly disoriented nano-
254 crystals of monazite; in Figures 8d and 5e some fringes can be observed within these bands. FFT of
255 different areas in Figure 8c show the strong disorientation from the [100] direction (FFT1) depending
256 on position in the band (compare FFT2 and 3 in Fig. 8c). In FFT3 the area is strongly disoriented with

only a faint (0-11) reflection visible. Extra spots observed at 3.58 Å in SAED in TEM mode (Fig. 7e) are also visible (arrows in FFT2), and appear when crossing the band (see arrows in FFT2).

3.3.3. TEM foil of naturally shocked Vredefort monazite – Figure 9 (and Supplementary Data S2; Figures S9)

One FIB-foil located across deformation twins (FIB4 in S9a) was prepared from one area of Vredefort monazite Sec-03D, grain 9 (*Cavosie et al., 2018*). Only deformation twins (Fig. 9), have been observed. Some twins are visible along the (001) plane (Fig. 9a-b). The (001) deformation twins are consistent with those reported from prior EBSD analysis (*Cavosie et al., 2018*). Twins along the (001) plane range from 250 nm to 1.1 µm in width, and contain an enrichment in Ca along the twin-host boundary but no enrichment nor depletion of Pb (Fig. 9c-d and S9b in Supplementary data).

4. Discussion

4.1. Experimental shock-deformation features up to the nanoscale.

Early shock experiments on monazite (up to 59 GPa) used the shock-wave reverberation technique and high explosives for planar shock-wave generation (*Deutsch and Schärer, 1990)*; the shocked monazite grains exhibited lower birefringence, decolorization, intense mosaicism and the presence of fractures. Laser shock experiments on monazite by femtosecond laser ablation show the effect of high-pressure shock waves caused by plasma expansion, revealing nanostructural deformation features below the ablation crater, including fractures, mosaïcism, and deformation twins (*Seydoux-Guillaume et al., 2010; D'Abzac et al., 2012*). Static experimental data (using diamond anvil cell) focused on high-pressure transformation of monazite with various compositions ($CePO_4$-*Huang et al., 2010*; $SmTbPO_4$-*Heuser et al., 2018;* La, Nd, Eu, $GdPO_4$-*Lacomba-Perales et al., 2010*). *Huang et al. (2010)* revealed only structural lattice distortion at around 11 GPa, with no phase transition up to 20 GPa. In contrast, *Lacomba-Perales et al. (2010)* identified a non-reversible high-

pressure phase with barite-type structure at 26 GPa for $LaPO_4$ but no phase transition up to 30 GPa for other compositions (Gd, Eu, $NdPO_4$).

In the present study, no significant difference between Raman spectra was observed between unshocked and shocked monazite samples, except for the structural distortion responsible for both Raman-band broadening and data spreading; hence no evidence for formation of a high-pressure phase was found (Fig. 2). Raman-band broadening of natural monazite is due to the combination of two effects: chemical composition (mostly Th, U, Ca and Pb) and lattice distortion caused by radiation damage *(e.g. Nasdala et al., 2002; Seydoux-Guillaume et al., 2002; Ruschel et al., 2012). Ruschel et al. (2012)* proposed an empirical formula for estimating the degree of radiation damage if the chemical composition is known:

$$FWHM\ [cm^{-1}] = 3{,}95 + 26{,}66 \times (Th+U+Ca+Pb)\ [apfu]$$

where FWHM is the full width at half maximum of the most intense Raman band of monazite (i.e., the ν_1 symmetric PO_4 stretching mode near 970 cm^{-1}; Fig. 2). The monazite used for our experiments contains 0.12, 0.002, 0.045, and 0.003 apfu (based on 4O) for Th, U, Ca and Pb respectively, which gives a ∑(Th+U+Ca+Pb) of 0.17 apfu (*Seydoux-Guillaume et al., 2004*). The expected FWHM is then 8.5 cm^{-1} for monazite with the same composition and no radiation damage. The FWHM of the unshocked monazite is 18.3 cm^{-1}. Interestingly, the monazite used in the present study corresponds closely to the F6 monazite described in *Ruschel et al. (2012)*, with a ∑(Th+U+Ca+Pb) of 0.15, a $FWHM_{unannealed}$ of 18.1 cm^{-1} and a $FWHM_{annealed}$ of 7.9 cm^{-1}. The difference in width of Raman peaks between $FWHM_{unannealed/unshocked}$ (18.1 and 18.3 cm^{-1}) values to $FWHM_{annealed}$ (7.9 and 8.5 cm^{-1}) values is attributed to the "radiation damage component" (~10 cm^{-1}). The FWHM of Raman-bands from the shocked monazite domains C1 and C2 are ~21.5 cm^{-1} (Fig. 2). The ~3 cm^{-1} difference in the FWHM of the Raman band between the unshocked and shocked monazite is attributed to shock-induced distortion of the lattice. The FWHM increase is expected when grain size is reduced, as broadening is inversely proportional to grain size in CeO_2 ceramics (e.g., *Gouadec and Colomban, 2007*). In ceria,

band broadening of 3 cm^{-1} is observed for grain size of about 40 nm, thus the observed broadening of 3 cm^{-1} is consistent with the TEM observation of mosaicism at a similar scale (Fig. 3 and 6).

Raman band broadening here is essentially related to two nano-features identified using TEM: mosaicism (Figs. 3 and 6) and the presence of planar band structures (Figs. 4 and 7). As the unshocked monazite crystal already contains radiation damage, expressed as typical mottled diffraction contrasts in BF-TEM mode and corresponding to small lattice distortion and the presence of strain (*Seydoux-Guillaume et al., 2002; 2004; 2018*), it is not obvious how to isolate the "radiation damage component" from the "shock component", as done in the previous paragraph with Raman. The role of radiation damage, and therefore the role of "initial structural state" of monazite at time of impact, and formation of shock-deformation features, is discussed below. As the unshocked monazite was previously well-characterized, it is here possible to distinguish some of the shock effects. Note especially BF-TEM images in *Grand'homme et al. (2018),* Figures 7, 9 and 10 (Mnz1). Mosaicism was absent in the pristine monazite crystal (*Seydoux-Guillaume et al., 2004*). Conspicuous streaking in the diffraction spots, moiré fringes, and the presence of extra diffraction spots in the SAED pattern, are all evidence that the monazite nanodomains are misorientated by a few degrees, i.e. mosaicism.

The deformation bands (Figs. 4 and 7) have not been observed in monazite before, even in shocked samples from femtosecond-laser experiments (*Seydoux-Guillaume et al.,2010*; *d'Abzac et al. 2012)*; this microstructure unambiguously formed in response to the shock experiment. The orientation of the deformation bands is parallel to the direction of shock wave propagation into the crystal (Figs. 4a-b and 7). They are different from typical planar deformation features (PDF) classically observed in shocked silicates by TEM like quartz (*Langenhorst and Deutsch, 2012*) or zircon (*Reimold et al., 2002; Leroux et al., 1999*), which are straight, sharp and continuous planes, filled with amorphous material, and sometimes decorated by bubbles formed during post-shock processes, such as annealing or alteration (*Langenhorst and Deutsch, 2012).* In the studied shocked monazite, the band structures are shorter (hundreds of nm long) and are not filled with an entirely amorphous material but instead are defined by nanometer sized domains with a highly different orientation, as shown in

STEM-ADF images (Fig. 8c-e and in the various FFT from Fig. 8c). This observation is also confirmed by the presence of diffraction contrasts in BF-TEM (Fig. 7c-d), a SAED pattern which shows almost no diffuse diffraction ring (Fig. 7e) but instead contains extra spots characteristic of a monazite lattice, and streaking of spots corresponding to high misorientation of nanodomains to each other and from orientation of the monazite host. We suggest that such features may represent precursor microstructural damage that leads to formation of more typical features found in shocked monazite, such as planar deformation bands (e.g. *Erickson et al., 2016)*. Another possibility is that they represent partly annealed PDFs, similar to those described in various shocked minerals (e.g. *Leroux et al., 2001*), which do not remain amorphous after shock due to the ability of monazite to recrystallize in response to thermal and/or ionization processes (*Seydoux-Guillaume et al., 2004 and 2018*). These highly misoriented deformation band structures could also represent domains from which either neoblasts or a high-pressure phase could crystallize in natural shocked monazite. Additional diffraction spots observed within these domains can all be attributed to the monazite lattice (Figs. 7d-e), and thus might also represent incipient formation of neoblasts.

4.2. Laser-shock experiments as analogues for naturally-shocked samples

One of the main objectives of the present study is to evaluate if laser-driven shock experiments reproduce the types of impact damage previously characterized in naturally shocked monazite. Shocked monazite has been reported both in bedrock of the Vredefort impact structure, South Africa (*Moser, 1997, Erickson et al., 2017*), the Nördlinger Ries crater, Germany, the Haughton dome, Canada (*Erickson et al., 2019*), the Araguainha crater, Brazil (*Erickson et al., 2017*), the Woodleigh impact structure in Australia (*Fougerouse et al., 2021a*), the Yarrabubba monzogranite and Barlangi granophyre impact melt (*Erickson et al., 2020*), and in both modern and Pleistocene alluvial deposits of the Vaal River in South Africa as detrital grains (*Cavosie et al., 2010; Erickson et al., 2013; Cavosie et al., 2018*). *Erickson et al. (2019)* reported shocked monazite grains from Ries Crater and Haughton dome with complex yet systematic twin relations produced by reversion from an

unquenchable high-pressure tetragonal polymorph, a phase not previously known. No studies have investigated shock-deformation structures in monazite at a nanometer scale, except a recent study by *Fougerouse et al. (2021a)* that focused on Pb mobility as determined from atom probe tomography, a method shown previously to demonstrate atom-scale element mobility or segregation on twin boundaries triggered by tectonic deformation (*Fougerouse et al., 2021b*).

The results presented here demonstrate the ability of laser-driven experiments to produce shock deformation microstructures previously described in the literature,, specifically mosaïcism, and deformation bands. Additional microstructures described by *Cavosie et al. (2018) and Erickson et al. (2017)* include deformation twinning (Fig. 9) and neoblastic domains.. We suggest that the highly-deformed bands may represent either precursor microstructural damage that leads to formation of more typical features found in naturally shocked monazite, such as planar deformation bands (e.g. *Erickson et al., 2016)* or deformation twins, which failed to form during the experiment, likely because of insufficient duration of pressure application. The presence of neoblastic domains provides evidence of localized recrystallisation of monazite during, or more likely, immediately following shock deformation. The absence of neoblasts in the laser shock-loaded monazite crystal may be explained by either (i) lower shock conditions, too low to induce recrystallization, in contrast to what can be observed in naturally shocked monazite (e.g. *Erickson et al., 2017; 2020*), or by (ii) insufficient duration of the thermomechanical load, shorter by many orders of magnitude in the experiment (~6 ns-pressure pulse, see Section 2.2), which may be below the characteristic time required to form neoblasts.

4.3. Role of radiation damage in formation of shock-deformation features?

In order to ascertain shock conditions of minerals during impact events, the structural state of the mineral at the time of impact must be estimated. In the case of zircon, a mineral highly sensitive to radiation damage, formation of the high-pressure polymorph reidite is inhibited in partially metamict zircon due to the general reduction in longitudinal and shear stiffness with radiation damage

(*Erickson et al., 2017; Timms et al., 2018*). Extrapolation of impact conditions in natural shocked zircon can thus be complicated due to lack of knowledge of pre-impact intrinsic properties. In contrast, monazite has the ability to remain crystalline over geological time due to self-annealing of radiation damage (*Seydoux-Guillaume et al. 2004; 2018b*), however it is not known if the presence of radiation damage influences formation of shock-deformation features or high-pressure polymorphs (e.g., *Erickson et al., 2019*). Further shock-experiments using monazite free of radiation damage as a starting material may be able to elucidate such behavior.

It is also worth considering that monazite samples older than 1 Ga may have accumulated a high amount of radiogenic Pb in the lattice and received intensive radiation doses. Even if clear evidence for radiation damage is limited to nm-isolated domains within monazite resulting in lattice distortion (*Seydoux-Guillaume et al., 2004*), these effects induce Raman broadening and mottled diffraction contrasts visible in TEM. At the micrometer scale, peak broadening of Raman spectra provides one indication that monazite crystals were affected by a shock event. This requires, however, knowledge of both composition and FWHM of Raman spectra of unshocked monazite samples, in order to evaluate the radiation damage component, which produces the same broadening effect (*Nasdala et al., 2002; Seydoux-Guillaume et al., 2002; Ruschel et al., 2012*). More investigations using TEM are needed to confirm a primary (shock) interpretation, and to describe in detail shock deformation features. Analysis of shocked monazite by TEM revealed intense lattice distortion in the form of mosaicism, deformation bands, and the presence of intense streaking and extra spots in the SAED pattern; these features can unambiguously be attributed to deformation that occurred during the experimental shock loading experiment. Unshocked monazite crystals (e.g. *Seydoux-Guillaume et al., 2004 and 2018a)* and tectonically deformed grains (*Fougerouse et al., 2021b*), did not display Bragg diffraction contrasts in bright field mode (with their corresponding SAED patterns) as pronounced as those described here that correspond to mosaïcism and deformation bands. Inside the twinned areas (Fig. 9) it is almost impossible to distinguish contrasts in shocked monazite from those of tectonically deformed monazite, except in the case where twin orientations are specifically characteristic of shock

deformation (*Erickson et al., 2016*; *Fougerouse et al., 2021a*). However, in the case of common twin orientations, this criterion is not sufficient.

CONCLUSIONS

This study demonstrated the ability of laser-driven shock experiments using a high-energy laser pulse of ns-order duration to produce shock-deformation microstructures observed in natural shocked monazite. We describe two main microstructural features at the nanoscale: mosaïcism, and deformation bands. Both mosaïcism and deformation bands, expressed in SAED patterns with streaking of spots, and the presence of extra spots, more or less pronounced, provide evidence to identify shocked monazite grains. Other shock-deformation features reported in naturally shocked monazite, such as deformation twins, high-pressure polymorphs and neoblastic domains, were not observed in the experimental charges. Further study is needed to evaluate the possibility of forming such features with laser-driven shock experiments. Furthermore, as the presence of radiation damage may also modify the formation of shock-deformation features, use of monazite crystals free of radiation damage may help to answer this question.

Acknowledgments

This project has received financial support from the CNRS through the INSU-PNP, the MITI interdisciplinary programs and the IEA Nanomobility. The CLyM (Consortium Lyon St-Etienne de Microscopie) is thanked for access to the TEM NeoARM in Saint-Etienne (France). The Raman facility in Lyon (France) is supported by the Institut National des Sciences de l'Univers (INSU). It is a contribution of the LABEX Lyon Institute of Origins (ANR-10- LABX-0066), within the program "Investissements d'Avenir" (ANR-11-IDEX-0007) at Université de Lyon. AJC acknowledges funding from the Space Science and Technology Centre at Curtin University. We thank the editor William B. McKinnon and reviewer Axel Wittmann for valuable comments that greatly improved the final version of this manuscript.

437

438 **References**

439 Cavosie, A.J., Erickson, T.M., Montalvo, P.E., Prado, D.C., Cintron, N.O. and Gibbon, R.J. (2018). The
440 Rietputs Formation in South Africa. In: Microstructural Geochronology (eds D.E. Moser, F. Corfu,
441 J.R. Darling, S.M. Reddy and K. Tait), 203-224. https://doi.org/10.1002/9781119227250.ch9

442 Cavosie, A.J., Kirkland, C.L., Reddy, S.M., Timms, N.E., Talavera, C., and Pincus, M.R. (2021). Extreme
443 plastic deformation and subsequent Pb loss in shocked xenotime from the Vredefort Dome, South
444 Africa . In Large Meteorite Impacts and Planetary Evolution VI : Geological Society of America
445 Special Paper (eds Reimold, W.U., and Koeberl, C.), 550, 465-478.

446 Cavosie, A.J., Quintero, R.R., Radovan, H.A., and Moser, D.E. (2010). A record of ancient cataclysm in
447 modern sand: shock microstructures in detrital minerals from the Vaal River, Vredefort Dome,
448 South Africa. Geological Society of America Bulletin, v. 122, p. 1968–1980.

449 D'Abzac, F.-X., Seydoux-Guillaume, A.-M., Chmeleff, J., Datas, L., Poitrasson, F. (2012) In situ
450 characterization of infrared femtosecond laser ablation in geological samples. Part A: the laser
451 induced damage. Journal of Analytical Atomic Spectrometry 27, 99–107.

452 Du, A., Wan, C., Qu, Z. and Pan, W. (2009). Thermal conductivity of monazite-type $REPO_4$ (RE=La, Ce,
453 Nd, Sm, Eu, Gd). Journal of the American Ceramic Society, 92, 2687-2692.
454 https://doi.org/10.1111/j.1551-2916.2009.03244.x

455 Erickson, T.M., Kirkland, C.L., Timms, N.E., Cavosie, A.J. and Davison, T.M. (2020) Precise radiometric
456 age establishes Yarrabubba, Western Australia, as Earth's oldest recognized meteorite impact
457 structure. Nature Communication 11(1), 1-8.

458 Erickson, T.M., Timms, N.E., Kirkland, C.L., Tohver, E., Cavosie, A.J., Pearce, M.A. and Reddy, S.M.
459 (2017) Shocked monazite chronometry: integrating microstructural and in situ isotopic age data
460 for determining precise impact ages. Contribution to Mineralogy and Petrology 172(2-3), 11.

461 Erickson, T.M., Timms, N.E., Pearce, M.A., Cayron, C., Deutsch, A., Keller, L.P. and Kring, D.A. (2019)
462 Shock-produced high pressure (La, Ce, Th) PO_4 polymorph revealed by microstructural phase
463 heritage of monazite. Geology 47(6), 504-508.
464 Erickson, T.M., Cavosie, A.J., Moser, D.E., Barker, I.R., Radovan, H.A., and 499 Wooden, J. (2013).
465 Identification and provenance determination of distally transported, Vredefort-derived shocked
466 minerals in the Vaal River, South Africa using SEM and SHRIMP-RG techniques. Geochimica et
467 Cosmochimica Acta, 107, 170-188.
468 Erickson, T.M., Cavosie, A.J., Pearce, M.A., Timms, N.E., Reddy, S.M. (2016). Empirical constraints of
469 shock features in monazite using shocked zircon inclusions. Geology, 44, 635-638.
470 Erickson, T.M., Pearce, M.A., Taylor, R.J.M., Timms, N.E., Clark, C., Reddy, S.M., and Buick, I.S. (2015)
471 Deformed monazite yields high-temperature tectonic ages. Geology, 43, 383–386,
472 https://doi.org/10.1130/G36533.1.
473 Ewing, R.C., Meldrum, A., Wang, L.M., Weber, W.J., Corrales, L.R. (2003). Radiation damage in zircon.
474 In: Hanchar, J.M., Hoskin, P.W.O. (Eds.), Zircon. Reviews in Mineralogy and Geochemistry, vol.53.
475 Mineralogical Society of America, pp.387–425.
476 Feng, J., Xiao, B., Zhou, R., and Pan, W. (2013). Anisotropy in elasticity and thermal conductivity of
477 monazite-type REPO4 (RE=La, Ce, Nd, Sm, Eu and Gd) from first-principles calculations. Acta
478 Materialia, 61, 19, 7364-7383. 10.1016/j.actamat.2013.08.043.
479 Fougerouse, D., Cavosie, A., Erickson, T., Reddy, S., Cox, M., Saxey, D., Rickard, W., Michael, T. and
480 Wingate, M. (2021a). A new method for dating impact events – Thermal dependency on nanoscale
481 Pb mobility in monazite shock twins. Geochim. Cosmochim. Acta, 314, 381-396.
482 https://doi.org/10.1016/j.gca.2021.08.025
483 Fougerouse, D., Reddy, S.M., Seydoux-Guillaume, A.-M, Kirkland, C.L., Erickson, T.M., Saxey, D.W.,
484 Rickard, W.D.A., Jacob, D., Leroux, H., and Clark, C. (2021b). Mechanical twinning of monazite
485 expels radiogenic Pb. Geology, 49, 417-421. https://doi.org/10.1130/G48400.1

Fougerouse, D., Reddy, S.M., Saxey, D.W., Erickson, T., Kirkland, C.L., Rickard, W.D.A., Seydoux-Guillaume, A.-M., Clark, C., and Buick, I.S. (2018). Nanoscale distribution of Pb in monazite revealed by atom probe microscopy. Chemical Geology, 479, 251-258. https://doi.org/10.1016/j.chemgeo.2018.01.020

French, B.M. and Koeberl, C. (2010) The convincing identification of terrestrial meteorite impact structures: what works, what doesn't, and why. Earth Science Review 98(1-2), 123-170.

Gardès, E., Montel, J.-M., Seydoux-Guillaume, A.M., and Wirth, R. (2007). Pb diffusion in monazite: New constraints from the experimental study of Pb^{2+} <=> Ca^{2+} Geochimica et Cosmochimimica Acta, 71, 4036-4043.

Gouadec, G., and Colomban, P. (2007). Raman Spectroscopy of nanomaterials: How spectra relate to disorder, particle size and mechanical properties. Progress in Crystal Growth and Characterization of Materials 53, 1-56

Grand'Homme, A., Janots, E., Seydoux-Guillaume, A.-M., Guillaume, D., Magnin, V., Hövelmann, J., Höschen, C., and Boiron, M.C. (2018). Mass transport and fractionation during monazite alteration by anisotropic replacement. Chemical Geology, 484, 51-68.

Hay, R.S., and Marshall, D.B. (2003) Deformation twinning in monazite. Acta Materialia, 51, 5235-5254.

Heuser, J.M., Palomares, R.I., Bauer, J.D., Lozano Rodriguez, M.J., Cooper, J., Lang, M., Scheinost, A.C., Schlenz, H., Winkler, B., Bosbach, D., Neumeier, S., Deissmann, G. (2018). Structural characterization of (Sm,Tb)PO4 solid solutions and pressure-induced phase transitions. Journal of the European Ceramic Society, 38, 11, 4070-4081.

Huang, T., Lee, J.-S., Kung, J., and Lin, C.-M. (2010). Study of monazite under high pressure. Solid State Communications, v. 150, p. 1845–1850, https:// doi .org /10 .1016 /j .ssc .2010 .06 .042 .

Jourdan, F., Reimold, W. U. and Deutsch, A. (2012) Dating terrestrial impact structures. Elements 8(1), 49-53.

Lacomba-Perales, R., Errandonea, D., Meng, Y., and Bettinelli, M. (2010). High-pressure stability and compressibility of *A*PO4 (*A* = La, Nd, Eu, Gd, Er, and Y) orthophosphates: An X-ray diffraction study

using synchrotron radiation. Physical Review B: Condensed Matter and Materials Physics, 81, 064113, https:// doi .org /10 .1103 /PhysRevB .81 .064113.

Lang, M., Zhang, F., Lian, J., Trautmann, C., Neumann, R., Ewing, R.C. (2008). Irradiation-induced stabilization of zircon (ZrSiO4) at high pressure. Earth and Planetary Science Letters, 269, 291-295. doi:10.1016/j.epsl.2008.02.027

Langenhorst, F., Boustie, M., Migault, A., Romain, J.P. (1999) Laser shock experiments with nanoseconds pulses: a new tool for the reproduction of shock defects in olivine. Earth and Planetary Science Letters 173, 333-342.

Langenhorst, F. and Deutsch, A. (2012) Shock metamorphism of minerals. Elements 8(1), 31–36.

Leroux, H. (2001). Microstructural shock signatures of major minerals in meteorites. *European Journal of Mineralogy* 13, 253–272.

Leroux, H., Reimold, W., Koeberl, C., Hornemann, U. and Doukhan, J.-C. (1999) Experimental shock deformation in zircon: a transmission electron microscopic study. Earth Planet. Sci. Lett. 169(3–4), 291–301.

Leroux, H., Reimold, W.U., and Doukhan, J.-C. (1994). A TEM investigation of shock metamorphism in quartz from the Vredefort dome, South Africa, Tectonophysics, 230, 223-239. https://doi.org/10.1016/0040-1951(94)90137-6.

Moser, D.E., Arcuri, G.A., Reinhard, D.A., White, L.F., Darling, J.R., Barker, I.R., Larson, D.J., Irving, A.J., McCubbin, F.M., Tait, K.T., Roszjar, J., Wittmann, A. and Davis, C. (2019). Decline of giant impacts on Mars by 4.48 billion years ago and an early opportunity for habitability. Nature Geoscience, 12, 522-527.

Nasdala, L., Wenzel, M., Vavra, G., Irmer, G., Wenzel, T., and Kober, B. (2001) Metamictisation of natural zircon: accumulation versus thermal annealing of radioactivity-induced damage. Contrib. Mineralogy and Petrology, 141, 125-144.

536 Nasdala, L., Lengauer, C.L., Hanchar, J.M., Kronz, A., Wirth R., Blanc, P., Kennedy, A.K., Seydoux-
537 Guillaume, A.M. (2002). Annealing radiation damage and the recovery of cathodoluminescence.
538 Chemical Geology, 191, 121-140.
539 Ni, Y., Hughes, J.M., and Mariano, A.N. (1995). Crystal chemistry of the monazite and xenotime struc-
540 tures. American Mineralogist, 80, 21-26, https://doi.org/10.2138/am-1995-1-203.
541 Paquette, J.L., and Tiepolo, M., 2007. High resolution (5 µm) U–Th–Pb isotope dating of monazite with
542 excimer laser ablation (ELA)-ICPMS. Chemical Geology 240, 222-237.
543 Peterman, E.M., Reddy, S.M., Saxey, D. W., Snoeyenbos, D.R., Rickard, W.D., Fougerouse, D. and
544 Kylander-Clark, A.R. (2016). Nanogeochronology of discordant zircon measured by atom probe
545 microscopy of Pb-enriched dislocation loops. Science Advance 2(9) e1601318.
546 Reimold, W.U., Leroux, H. and Gibson, R.L. (2002) Shocked and thermally metamorphosed zircon from
547 the Vredefort impact structure, South Africa: a transmission electron microscopic study. Eur. J.
548 Mineral. 14, 859-868.
549 Ruschel, K., Nasdala, L., Kronz, A., Többens D.M., Škoda R., Finger F., and Möller A. (2012). A Raman
550 spectroscopic study on the structural disorder of monazite–(Ce). Mineralogy and Petrology 105,
551 41-55. https://doi.org/10.1007/s00710-012-0197-7
552 Schmieder, M. and Kring, D.A. (2020) Earth's impact events through geologic time: a list of
553 recommended ages for terrestrial impact structures and deposits. Astrobiology 20(1), 91–141.
554 Seydoux-Guillaume, A.-M., Bingen, B., Bosse, V., Janots, E. and Laurent, A.T. (2018a). Transmission
555 Electron Microscope imaging sharpens geochronological interpretation of zircon and monazite. In:
556 Microstructural Geochronology (eds D.E. Moser, F. Corfu, J.R. Darling, S.M. Reddy and K. Tait), 261-
557 275. https://doi.org/10.1002/9781119227250.ch12
558 Seydoux-Guillaume, A.-M., Deschanels, X., Baumier, C., Neumeier, S., Weber, W.J., and Peuget, S.
559 (2018b). Why natural monazite never becomes amorphous: experimental evidence for alpha self-
560 healing. American Mineralogist, 103, 824-827. doi.org/10.2138/am-2018-6447

561 Seydoux-Guillaume, A.-M., Fougerouse, D., Laurent, A.T., Gardes, E., Reddy, S.M., Saxey, D.W. (2019).
562 Nanoscale resetting of the Th/Pb system in an isotopically-closed monazite grain: a combined Atom
563 Probe and Transmission Electron Microscopy study. Geoscience Frontiers, 10, 65-76.
564 https://doi.org/10.1016/j.gsf.2018.09.004.
565 Seydoux-Guillaume, A.-M., Freydier., R., Poitrasson, F., D'Abzac, F.-X., Wirth, R., Datas, L. (2010)
566 Dominance of mechanical over thermally induced damage during femtosecond laser ablation of
567 monazite. European Journal of Mineralogy 22, 235-244.
568 Seydoux-Guillaume, A.-M., Goncalves, P., Wirth, R. and Deutsch, A. (2003). TEM study of polyphasic
569 and discordant monazites: site specific specimen preparation using the Focused Ion Beam
570 technique. Geology, 31, 973-976.
571 Seydoux-Guillaume, A.-M., Wirth, R., Deutsch, A., and Schärer, U. (2004). Microstructure of 24-1928
572 Ma concordant monazites: implications for geochronology and nuclear waste deposits. Geochimica
573 et Cosmochimica Acta, 68, 2517-2527.
574 Seydoux-Guillaume, A.-M., Wirth, R., Nasdala, L., Gottschalk, M., Montel, J.-M. and Heinrich, W.
575 (2002). An XRD, TEM and Raman study of experimentally annealed natural monazite. Physics and
576 Chemistry of Minerals, 29, 240-253.
577 Timms, N.E., Erickson, T.M., Pearce, M.A., Cavosie, A.J., Schmieder, M., Tohver, E., Reddy, S.M.,
578 Zanetti, M.R., Nemchin, A.A. and Wittmann, A. (2017) A pressure-temperature phase diagram for
579 zircon at extreme conditions. Earth-Sci. Rev. 165, 185–202.
580 Timms, N.E., Healy, D., Erickson, T.M., Nemchin, A.A., Pearce, M.A. and Cavosie, A.J. (2018). Role of
581 Elastic Anisotropy in the Development of Deformation Microstructures in Zircon. In Microstructural
582 Geochronology (eds D.E. Moser, F. Corfu, J.R. Darling, S.M. Reddy and K. Tait).
583 https://doi.org/10.1002/9781119227250.ch8.
584 Wittmann, A., Kenkmann, T., Schmitt, R.T., and Stöffler, D. (2006) Shock-metamorphosed zircon in
585 terrestrial impact craters. Meteoritics & Planetary Science, 41, 433-454, doi:10.1111 /j.1945-
586 5100.2006.tb00472.x.

587

588 **Figure captions**

589 **Figure 1** - Monazite single crystal before and after shock experiment. a-d. Optical views (a-c: binocular
590 and d: reflected light) from the 3 mm shocked area (central zone). e-g: Secondary Electron Microscope
591 images from 2 areas in the central zone where characterizations were performed. Arrows point to
592 cracks induced by shock.

593 **Figure 2** – Raman spectra performed in unshocked and shocked (C1 and C2) domains from monazite
594 crystal. a- average and standard deviation of the Raman spectra per group. b- diagram showing the
595 FWHM (full width at half maximum) of the v1 peak as a function of its spectral position (in cm^{-1}). These
596 values were corrected for the apparatus function of the Raman instrument (*Nasdala et al. 2001*). The
597 peak positions and FWHM were determined without smoothing spectra and a linear baseline was used
598 in the spectral range 800-1200 cm^{-1}. The reproducibility is better than +/- 0.01 cm^{-1} and our
599 uncertainties on data are two magnitude lower than 1 cm^{-1}.

600 **Figure 3** – Transmission Electron Microscope (TEM) images performed in C1 (FIB1). a- Selected Area
601 Electron Diffraction (SAED) from area in b. b- Bright-Field (BF) TEM image. c- Dark-Field (DF) TEM
602 image using spot 2 (SAED in a). Note mottled diffraction contrasts (b), streaking of diffraction spots
603 (a), and extra spots DF1 (3.26Å) and DF2 (1.81Å) in [100] oriented SAED (a), characteristic features
604 from mosaïcism (misoriented subgrains visible in DF-TEM in c).

605 **Figure 4** – Bright (a-b) and Dark Field (d-f) TEM images, and Selected Area Electron Diffraction (SAED -
606 c) pattern from FIB-foil (FIB1-C1). Note the presence of band features almost parallel to each other (a-
607 b), and moiré fringes (arrows in b), in a domain that is deeper in the FIB foil than in Figure 3. The
608 crystallinity is very reduced inside these bands, with almost no Bragg contrasts (homogeneous grey –
609 e). SAED pattern (c) realized across one band and the monazite (inset in e) in zone axis [100], shows
610 streaking of some spots and a lot of extra spots (DF1: 3,26Å, DF2: 1,81Å, DF3: 2,06Å) proof for highly
611 disoriented domains (misoriented subgrains visible in DF-TEM in d-f).

612 **Figure 5** – Annular Dark Field Scanning TEM (STEM) images from FIB-foil (FIB1-C1) zoom in the band
613 domains. a-b Lower magnification images: band domains appear darker (less diffracting regions). c-d-
614 High resolution images. Note the crystallographic fringes still visible in the dark band domain (d and
615 e). The perfectly ordered ADF-STEM image in d shows arrangements of heavy atoms (e.g. Ce) in [100]
616 zone axis, in agreement with the crystallographic model. A Gaussian low-pass filter for noise reduction
617 was applied to high-magnification STEM images (c-d).
618 **Figure 6** – Bright Field Transmission Electron Microscope (BF-TEM) images (a-b and d) and Selected
619 Area Electron Diffraction (SAED – c and e) from FIB-foil (FIB5) prepared from C2 area - Mosaïcism.
620 Note mottled diffraction contrasts (a-b), streaking of diffraction spots (c), moiré fringes (arrows in d),
621 and extra spots in [100] oriented SAED (arrows in e), characteristic features from mosaïcism
622 (misoriented subgrains).
623 **Figure 7** – Bright Field Transmission Electron Microscope (BF-TEM) images (a-d) and Selected Area
624 Electron Diffraction (SAED - e) from FIB-foil (FIB5) prepared from C2 area - Highly-disoriented bands.
625 Note the presence of band features almost parallel to each other (a and b), in a domain that is deeper
626 in the FIB foil (a). Note a very reduced crystallinity inside these bands, with almost no Bragg contrasts
627 (homogeneous grey – c and d). SAED pattern (e) realized across one band and the monazite (inset in
628 d) in zone axis [100], shows streaking of some spots and a lot of extra spots (arrows in e) proof for
629 highly disoriented domains.
630 **Figure 8** – Annular Dark Field Scanning TEM (STEM) images from FIB-foil (FIB5) prepared from C2 area
631 in the highly-deformed bands domain. a- Low magnification ADF-STEM image showing the presence
632 of bands domains appearing darker (less diffracting regions). b- zoom in one band domain. c- Zoom in
633 area inset in b and three Fast Fourier Transform (FFT) from different domains in c showing contrasts
634 between the bright perfectly ordered domain (FFT1) and dark highly disoriented (FFT2 and 3) domains
635 (bands). Note arrow indicating extra spot in FFT2 (measured at 3.2 Å). d-e: zoom from image in c. Note
636 the crystallographic fringes still visible in the dark band domain (d and e). The perfectly ordered ADF-

637 STEM image in f shows arrangements of heavy atoms in [100] zone axis, in agreement with the
638 crystallographic model (see Supp data S2).
639 **Figure 9** - Bright Field TEM images (a), SAED patterns (b), and High Resolution ADF-STEM images (c-d)
640 from one FIB-foil prepared in one naturally shocked monazite grain (Mnz9-FIB4) from Rietputs
641 formation (South-Africa; *Cavosie et al., 2018*). Deformation twins in (001) with Ca enrichment within
642 the boundary (Ca map from inset in c). Details on location of FIB foil and on chemical mapping are
643 given in Supp. Data S2.
644 **Figures**
645 **Figure 1:**

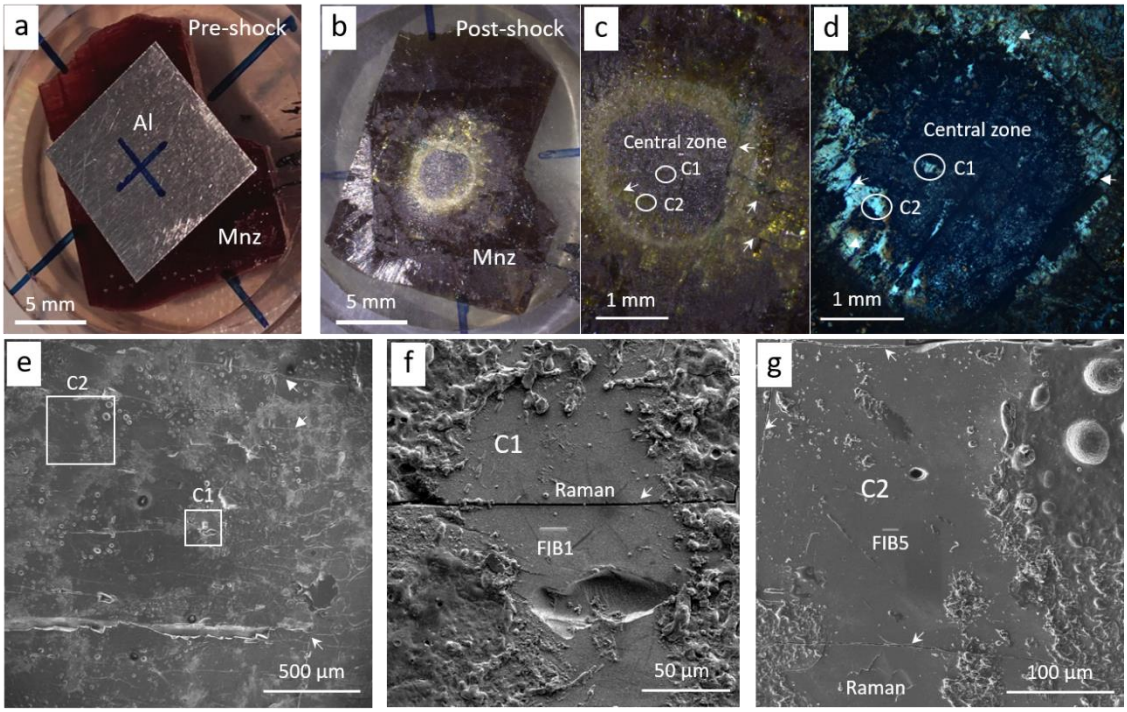

646
647 **Figure 2:**

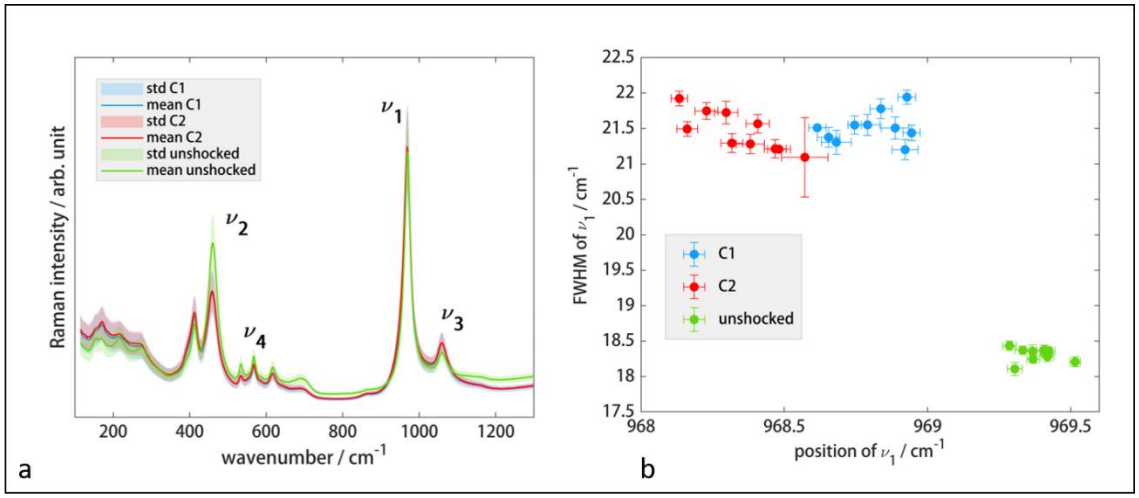

Figure 3:

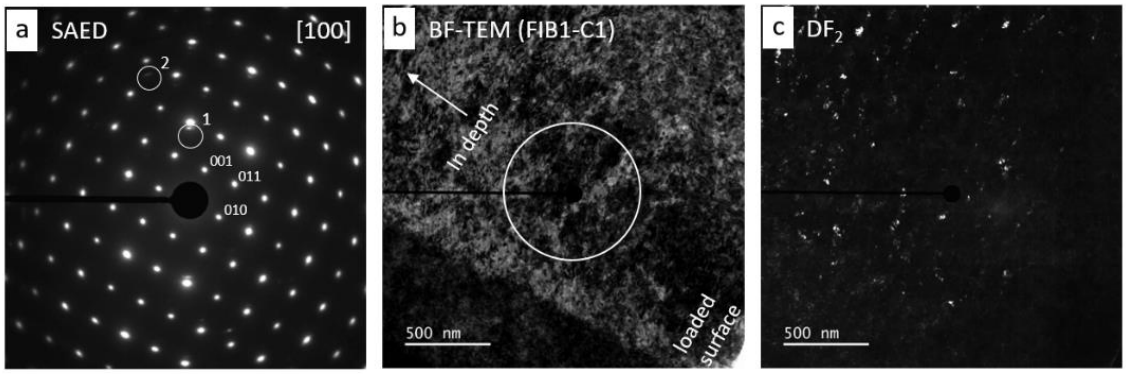

Figure 4:

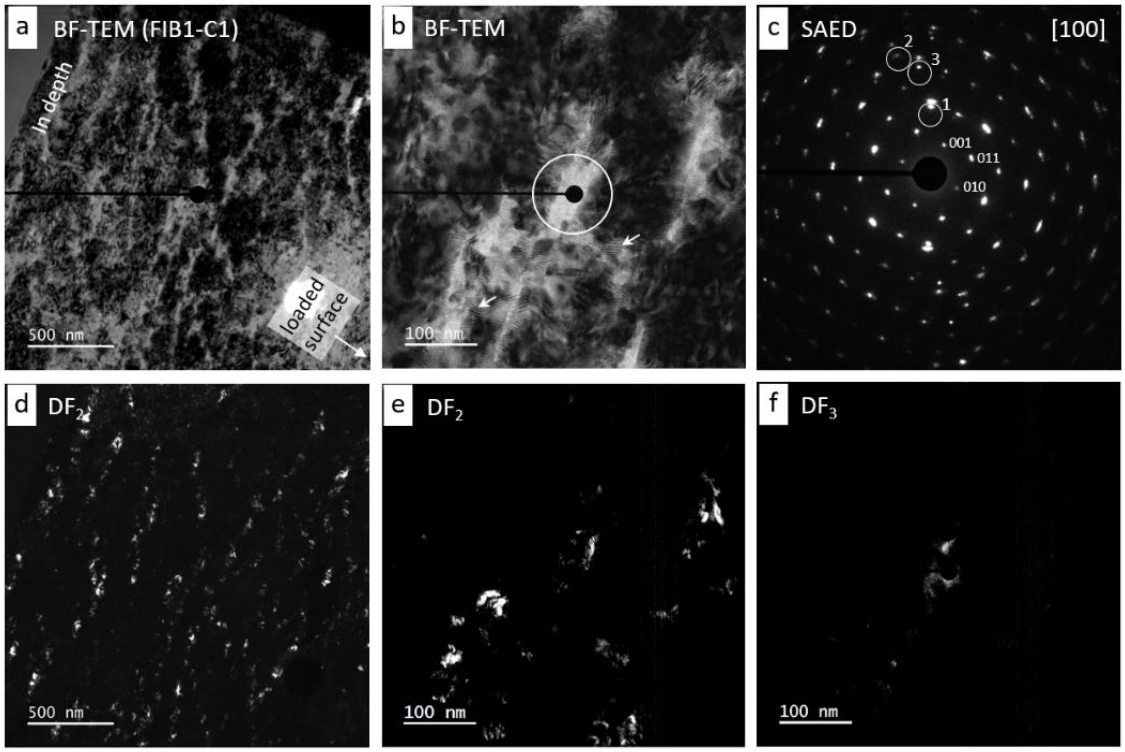

652

653 **Figure 5:**

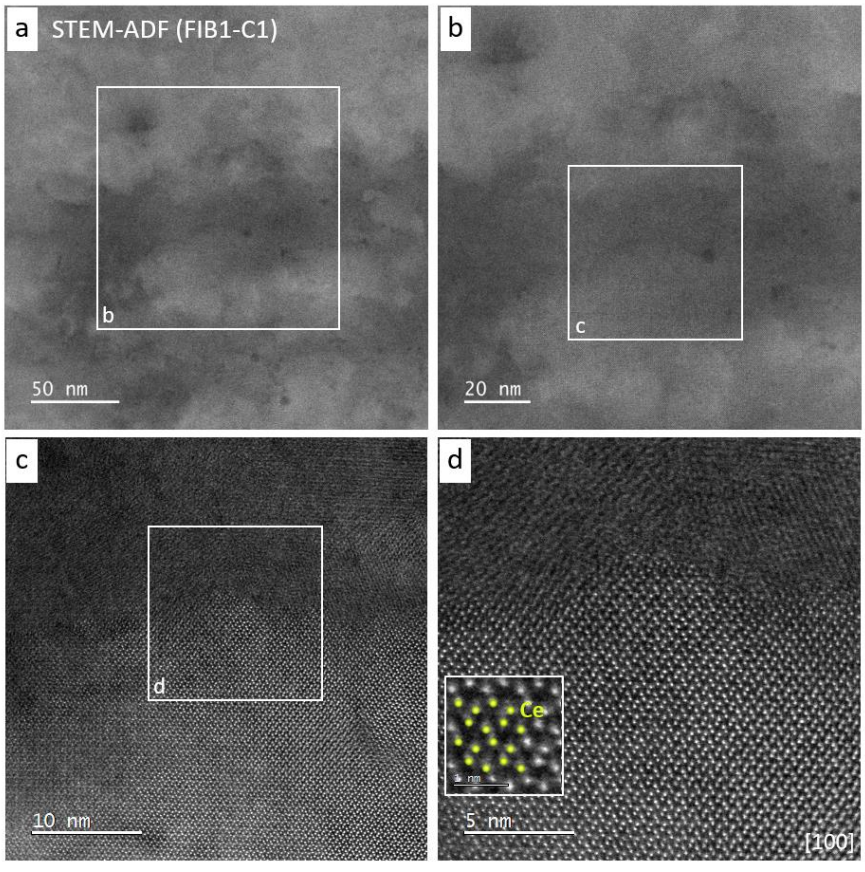

654

655 **Figure 6:**

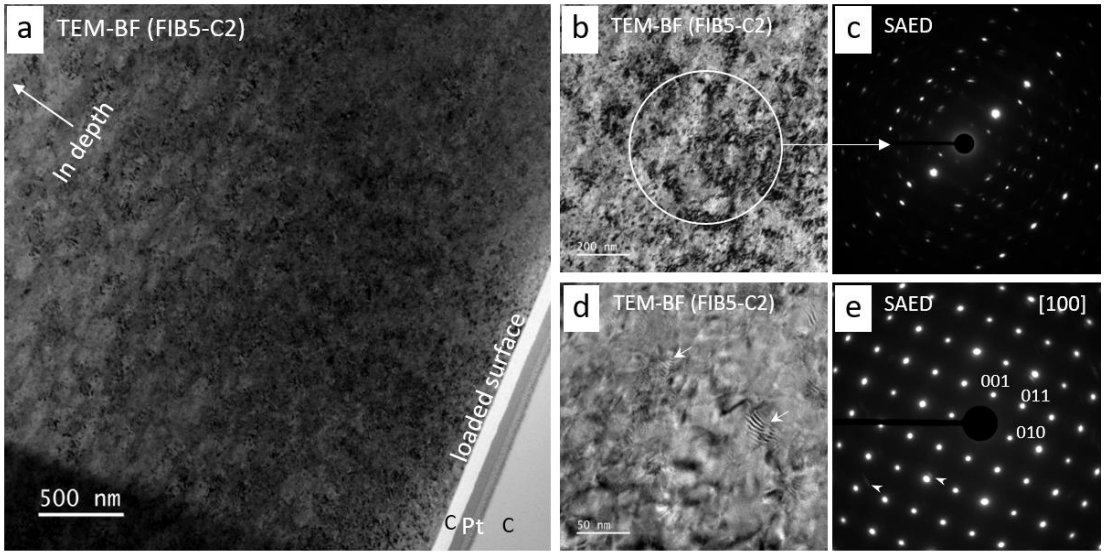

656

657 **Figure 7:**

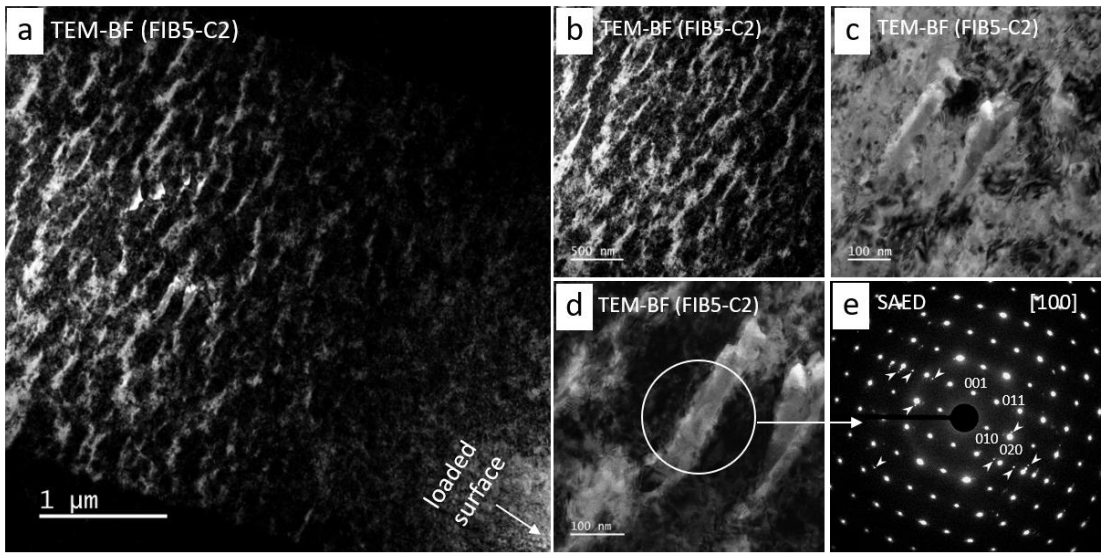

658

659 **Figure 8:**

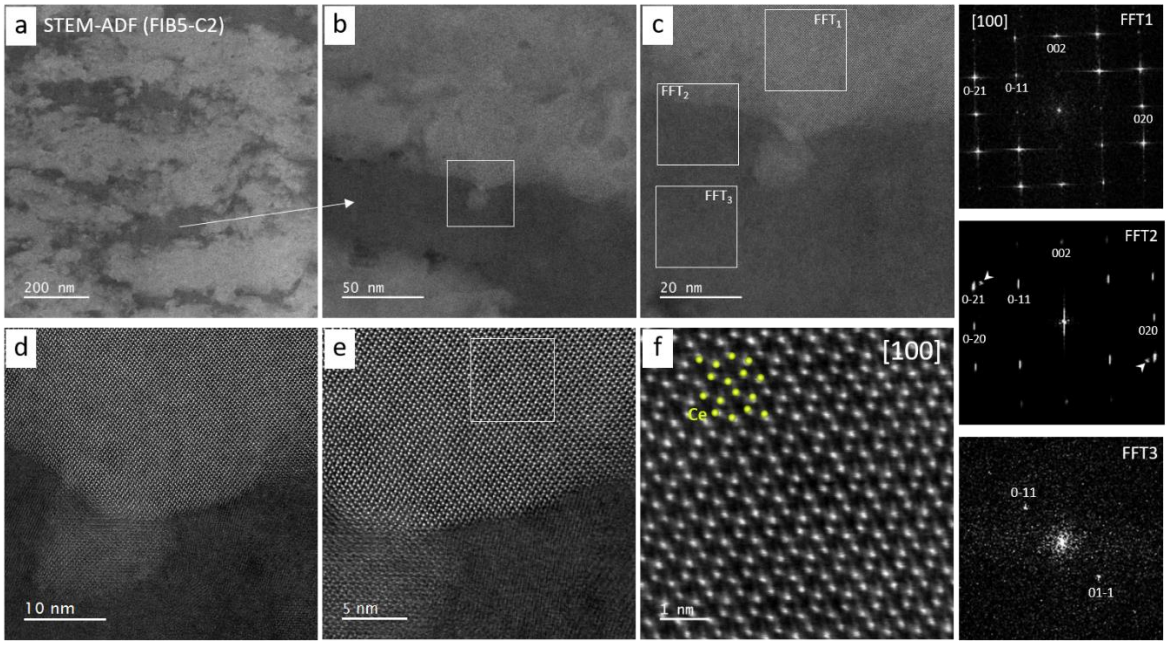

660

661 **Figure 9:**

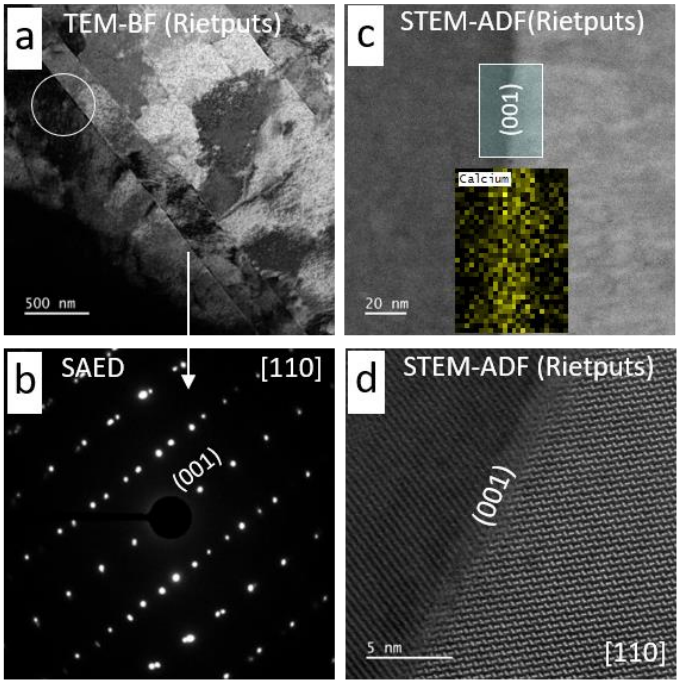

662